PAPER

Check for updates

Resolving local reaction environment toward an optimized CO₂-to-CO conversion performance†

Ke Ye,[a] Guiru Zhang,[a] Xian-Yin Ma,[b] Chengwei Deng,[c] Xin Huang,[a]
Chonghao Yuan,[a] Guang Meng,[a] Wen-Bin Cai[b] and Kun Jiang ⓘ ★[ad]

The local reaction environment, especially the electrode–electrolyte interface and the relevant hydrodynamic boundary layer in the vicinity of the cathode, plays a vital role in defining the activity and selectivity of the electrochemical CO₂ reduction reaction. Here, we present a differential electrochemical mass spectroscopic (DEMS) approach on the Ag electrode to resolve this information and provide hints for optimized CO₂-to-CO conversion performance. A multi-physics model with computational fluid dynamics and chemical simulation is firstly proposed to demonstrate the flow pattern and the CO₂ distribution within the cathodic DEMS chamber under operational conditions. Using this developed spectroelectrochemical method, we investigate the promotion effects of CO₂ mass transport, cation identity and surface topology on Ag catalyzed CO₂ reduction at a temporal resolution of ∼200 ms. As a proof of concept, these fundamental understandings have been validated in a pilot anion exchange membrane electrolyzer, leading to a CO partial current density above 650 mA cm⁻² at 4.0 V, an operational voltage window wider than 1.0 V and a stable CO generation for 100 hours at 500 mA cm⁻² for CO selectivity above 80%.

Broader context

In pursuit of a global transition from linear to circular carbon economy, electrochemically converting greenhouse gas CO₂ into carbon-based fuels and value-added chemicals using renewable energy sources has attracted considerable interest in past years, as a promising way to close the anthropogenic carbon cycle as well as to alleviate climate change. So far, this technique is largely challenged by its slow reaction kinetics of concerted proton-electron transfer and low conversion rate due to the evolution of dynamic reactive species and the resultant mass transport at the electrode–electrolyte interface. Targeted on efficient CO₂ electrolysis, leveraging *operando* spectroelectrochemistry to probe the interfacial information shall provide valuable hints on revealing the reaction mechanism and tuning up reaction performance. Inspired by these fundamental understandings, a variety of tuning knobs including catalyst structure, interfacial electric field, and mass/charge transport could be deployed toward an optimized electrolyzer performance. As such, the feedback loop between the fundamental surface electrochemical investigation and practical pilot device verification could envision the sustainable neutral carbon cycle.

Introduction

The electrochemical CO₂ reduction reaction (CO₂RR) driven by renewable electricity is a promising way to store intermittent powers and to convert greenhouse gas into fuels and commodity chemicals, holding the potential to close the anthropogenic carbon cycle.[1–4] Yet, major hurdles regarding relatively low energy efficiency and poor reaction selectivity should be properly addressed for the development of large-scale CO₂RR technologies.[5–7] The challenges arise from the strong competition of the hydrogen evolution reaction (HER) under the applied negative potentials, as well as the slow reaction kinetics of concerted proton-electron transfer steps.[8–10] Moreover, with negative-going potential sweep, significant concentration polarization is expected for the continuous consumption of both the proton and CO₂ reactant at the cathode surface from the bulk electrolyte, which largely hinders the electrocatalytic CO₂ conversion rate.[11,12]

Noteworthy, all the above challenges involve the electrode–electrolyte interface and relevant hydrodynamic boundary layer

[a] School of Mechanical Engineering, Shanghai Jiao Tong University, Shanghai 200240, China. E-mail: kunjiang@sjtu.edu.cn
[b] Shanghai Key Laboratory of Molecular Catalysis and Innovative Materials, Collaborative Innovation Center of Chemistry for Energy Materials, Department of Chemistry, Fudan University, Shanghai 200433, China
[c] State Key Laboratory of Space Power-Sources Technology, Shanghai Institute of Space Power Sources, Shanghai 200245, China
[d] Key Laboratory for Power Machinery and Engineering, Ministry of Education, Shanghai Jiao Tong University, Shanghai 200240, China
† Electronic supplementary information (ESI) available. See DOI: 10.1039/d1ee02966e

This journal is © The Royal Society of Chemistry 2022

Energy Environ. Sci., 2022, **15**, 749–759 | **749**

in the vicinity of the cathode. In past decades, novel catalyst design with delicate electronic structure control has been demonstrated as an effective way to tune up the intrinsic CO_2RR activity. Taken Ag, for example, opened surface sites and steps like Ag(211) surpass the close-packed terrace sites for electrocatalytic CO_2-to-CO conversion,[13,14] and compared to polycrystalline Ag foils, nanostructured Ag catalysts delivered an even higher CO generation performance due to their larger electrochemical surface area[15,16] and under the coordinated surface structure.[17,18] Broekmann *et al.* electrodeposited a nanofoam Ag catalyst with hierarchical porosity that delivers ~90% CO selectivity over a wide potential window from −0.3 V to −1.2 V *versus* the reversible hydrogen electrode (RHE).[19] This superior performance is attributable to the highly anisotropic, needle-shaped Ag feature with enlarged surface area, as well as the surface reconstruction from the reduction of surficial Ag_2O components. In addition to these intrinsic activity optimization strategies, the extrinsic reaction environment also plays an important role in determining CO_2RR activity and product selectivity. Under aqueous CO_2RR operation conditions, the hydrated cations will be migrated to the cathode, for which the cation identity and the resultant interfacial electric field are known with a significant impact on the activity of desired products.[20–22] More recently, Peters *et al.* reported the surface modification of a hydrophobic pyridinium layer on Ag that limits the diffusion rate of proton carriers but not CO_2, thus delivering a CO selectivity above 99% at −0.99 V.[23]

To directly probe the interactions of reactive species with their liquid reaction environment, developing *operando* methodologies and techniques are highly important but challenging to capture the real-time information on CO_2 reduction reactants, products, adsorbates and interfacial species evolution.[24,25] Intermittent online gas chromatography (GC)[26] and *ex situ* ^1H nuclear magnetic resonance (NMR)[27] are the two most widely adopted techniques for the quantification of gaseous and dissolved liquid products, respectively, providing an *ex parte* piece for this puzzle. So far, many efforts have been devoted to advancing the *operando* spectroelectrochemistry including but not limited to time-resolved attenuated total reflection infrared spectroscopy for the surface-bonded species analysis and shell-isolated nanoparticle-enhanced Raman spectroscopy for surface speciation detection.[28–30] Electrochemical mass spectrometry is another powerful tool for real-time detection of volatile species generated at the dependence of either potential sweep[31,32] or electrolyte switching.[33,34] Taking Cu-catalyzed CO_2RR as an example, Koper's group studied the possible intermediates for C_1 and C_2 pathways[35] and compared their structural sensitivity on probe-inlet online electrochemical mass spectroscopy (OLEMS) apparatus.[36] Later, a flow-cell design was proposed by Clark *et al.* to overcome the mass transport limitation from the probe tip in OLEMS,[37] an even higher detection efficiency was achieved by direct sampling of volatile species from the catalyst coated pervaporation membrane to the mass spectrometer.[11] More recently, a novel design of electron ionization quadrupole mass spectrometer

(EI-QMS) coupled with time-of-flight mass spectrometer (TOF-MS) system has been demonstrated,[38] the former is capable of detecting gaseous products while the latter is very efficient for nebulizing liquid product analysis in real-time. Thereafter, the transient information on the dynamic evolution of liquid products involving aldehydes and alcohols generated at Cu surfaces was clarified,[11,34,39] highlighting the importance of quantitative real-time measurements.

Herein, we deployed a membrane-inlet differential electrochemical mass spectroscopy (DEMS) apparatus to systematically screen the local reaction environment impact on Ag catalyzed CO_2 reduction performance. Using a combined hydromechanics and electrochemistry approach, highly sensitive detection, and quantification of gaseous CO and H_2 products was been achieved at a time resolution of ~200 ms. Over 95% CO selectivity can be achieved on the Ag surface *via* the electrolyte and the electrode topology optimization in a customized DEMS reaction cell. Moreover, this fundamental knowledge has been successfully transferred into practical CO_2RR operation on a membrane electrode assembly electrolyzer, delivering a CO partial current density over 650 mA cm^{-2} at a cell voltage of 4 V, and a long-term stable operation of 500 mA cm^{-2} at ~3.5 V for 100 h with CO selectivity above 80%.

Results and discussion

DEMS flow cell design and simulation

Fig. 1a depicts the construction of a homemade membrane-inlet DEMS flow cell. A catalyst-coated microporous PTFE membrane was deployed for pervaporation and directly served as the working electrode, for which the catalyst layer was exposed to cathodic electrolyte flow and the backside was supported by a stainless-steel frit connected to the vacuum system. To alleviate the mass transport limitation and the turbulence of bubbles in classic thin-layer flow cells,[40,41] we used the total catholyte volume as 0.9 mL and the anolyte volume as 0.6 mL. The electrolyte circulation in each chamber was controlled by an individual peristaltic pump and was separated by a Nafion 212 membrane.

The flow pattern and residence time of the catholyte within the working electrode chamber play an important role in determining the CO_2RR process and product collection efficiency using a quadrupole mass spectrometer.[37] Therefore, we first carried out a three-dimensional computational fluid dynamics simulation in COMSOL Multiphysics to identify the optimal flow field and mass transport. The flow pattern of capillary-inlet catholyte was determined by the Reynolds number (Re) as the following:

$$Re = \rho v l / \mu \qquad (1)$$

where ρ is the density of the fluid, v is the velocity, l is the characteristic length that is equal to the diameter of the capillary tube, and μ is the dynamic viscosity. Typical flow field visualization at a given flow rate of 128 mL min^{-1} is plotted in Fig. 1b, for which the k–ω turbulence model is deployed due to

750 | *Energy Environ. Sci.*, 2022, **15**, 749–759

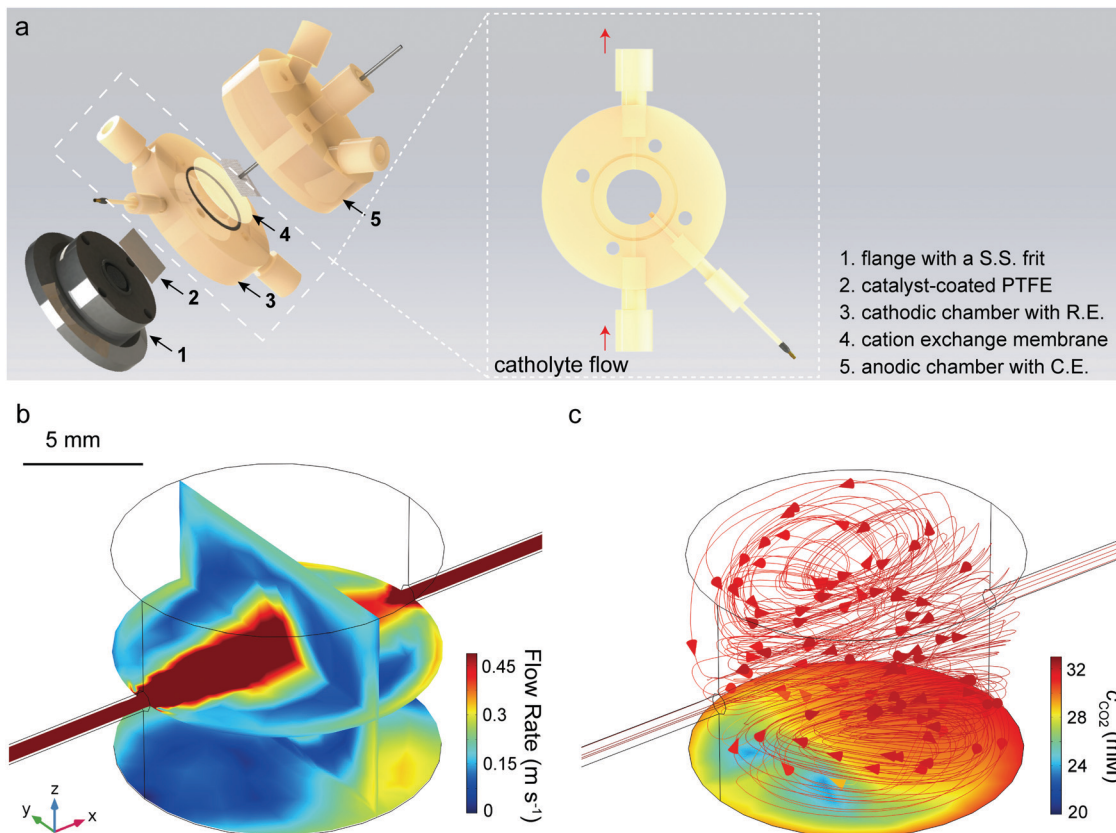This journal is © The Royal Society of Chemistry 2022

Fig. 1 Flow cell design for on-line DEMS investigation. (a) The explosion view of a homemade flow cell, together with the zoom-in view of the cathodic chamber. (b) Simulated catholyte flow field and (c) corresponding CO_2 concentration distribution at j_{CO} of 11 mA. 0.1 M CO_2-saturated $KHCO_3$ at a flow rate of 128 mL min^{-1} is chosen as the catholyte stream.

the calculated Re of 6726 and the corresponding pattern of jet flow.[42,43] It is noted that the electrolyte flow rate in the vicinity of the working electrode decreased significantly from the inlet velocity near the capillary, ensuring a normal electrochemical response (*vide infra*). The relevant CO_2 concentration profile at a given j_{CO} of 11 mA, a typical current density at −1.4 V *versus* RHE, is shown in Fig. 1c, the significant recirculation eddies in the bulk chamber help to alleviate the CO_2 mass transport limitation at the electrode surface, especially for the large flow rate used in our work compared to earlier dropwise electrolyte flow in a traditional thin-layer flow cell (Fig. S1, ESI†).

Ideally, the catholyte residence time should be equivalent to the acquisition time interval of mass spectrometry. A large residence time arising from the low flow rate is helpful for product detection but at the sacrifice of reactant supply, while a large flow rate may leave insufficient time for the detection of the accumulated CO_2RR products.[37] In practice, the mean residence time (τ) of interested species is dependent on the flow path, recirculation and dead zone within the nonideal reactor.[44] To accurately characterize τ, the cumulative distribution function $F(t)$ and the residence time distribution function $E(t)$ are evaluated as the following:

$$F(t) = c_t/c_0 \tag{2}$$

$$E(t) = \mathrm{d}F(t)/\mathrm{d}t \tag{3}$$

where c_0 is the initial inlet concentration of a tracer and c_t is the accumulated concentration at the outlet zone. We consider two different ways of tracer's injection, *i.e.*, the pulse input and the step input, to simulate the mean residence time (Fig. S2, ESI†):

$$\tau = \int_0^\infty tE(t)\mathrm{d}t \tag{4}$$

As a result, the determined τ value of catholyte within our customized flow reactor is determined as 0.16–0.17 s at a given flow rate of 128 mL min^{-1}, close enough to our DEMS sampling interval of ~ 0.2 s, thus enabling the balance optimized mass transport and detection sensitivity.

Quantification method for DEMS

To show the potential of the DEMS system, we tackled the effect of local reaction environment tuning on Ag toward CO_2RR performance upon switching electrolyte and electrode compositions. Fig. 2a and b show the morphology of sputtered Ag on PTFE at different scales before and after electrochemical CO_2RR measurements. A 400 nm Ag layer was homogeneously coated on PTFE fibers and roughened nanoparticles were observed after electrochemical reactions, in both cases, the microporous feature was largely maintained for pervaporation of further products and DEMS detection.[11]
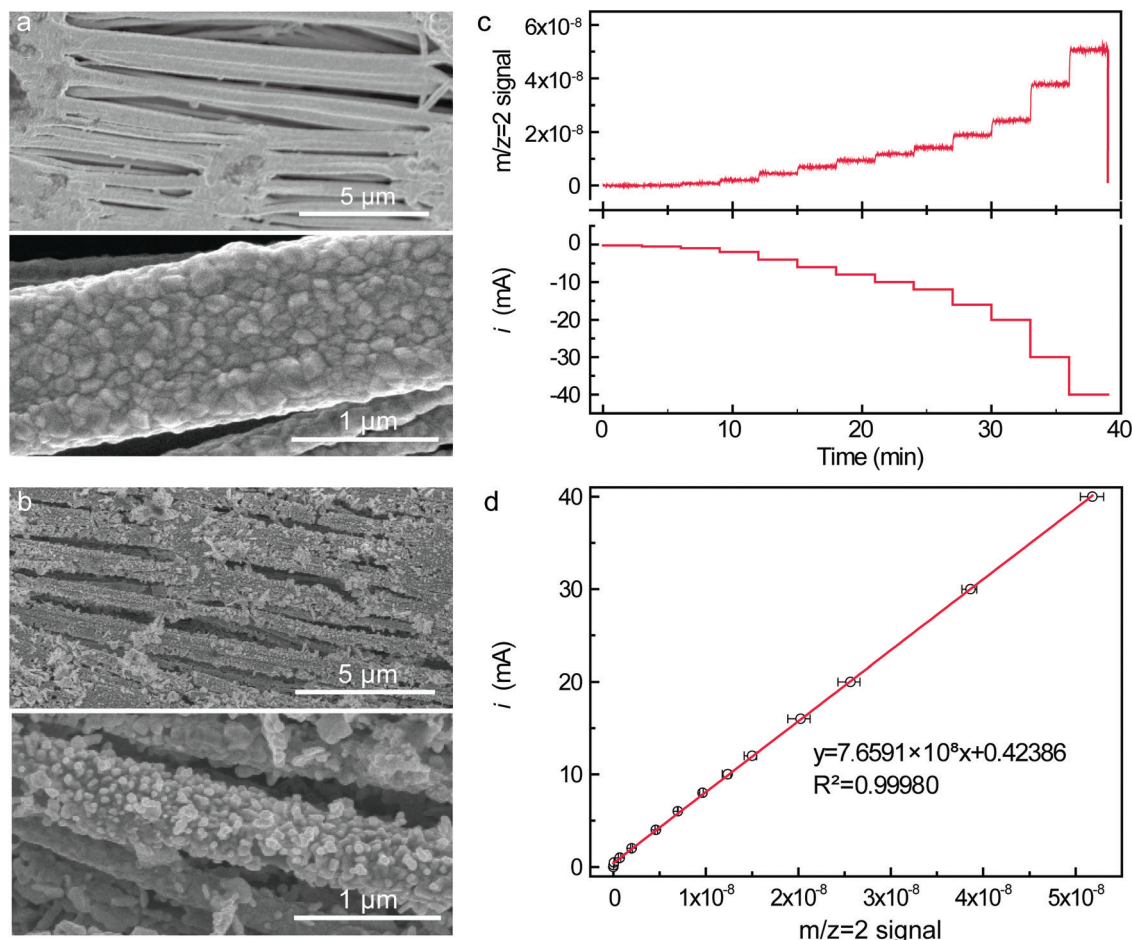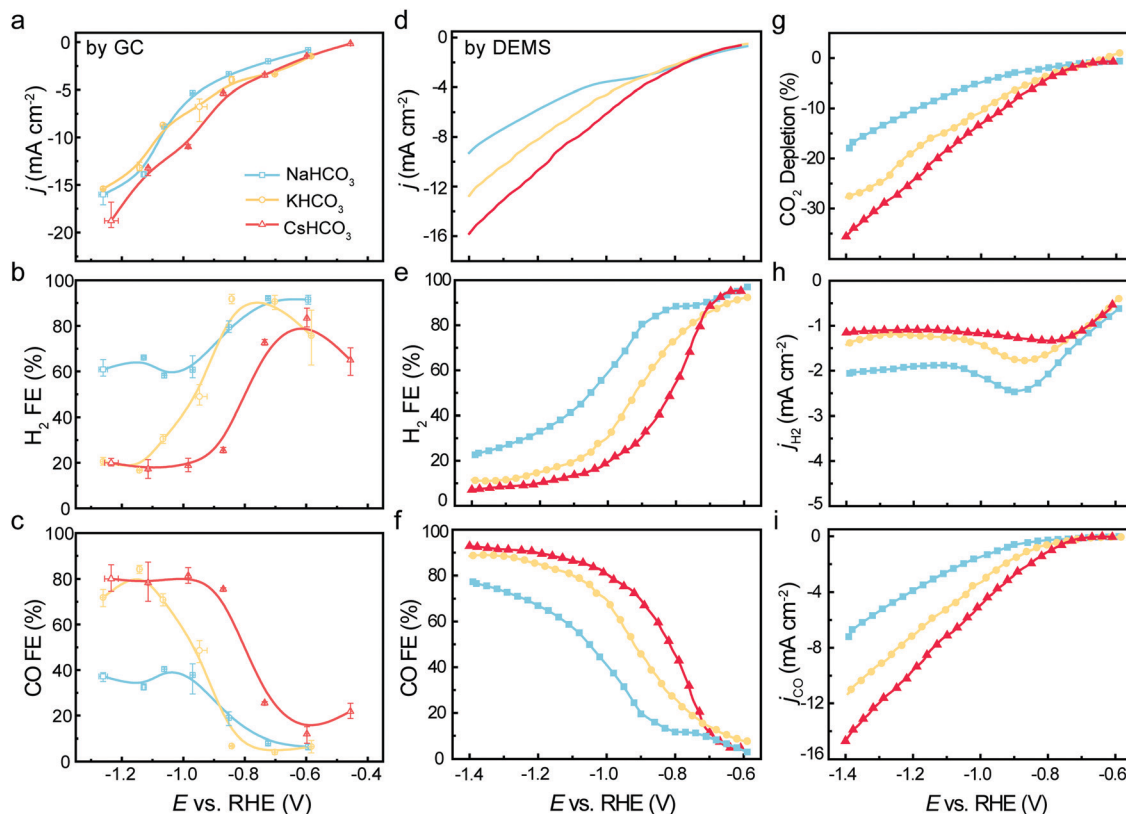
This journal is © The Royal Society of Chemistry 2022

Energy Environ. Sci., 2022, **15**, 749–759 | **751**

Fig. 2 Morphology characterization of sputtered Ag electrode and relevant calibration curves for the hydrogen evolution reaction (HER). (a) Scanning electron microscope (SEM) images of the pristine Ag electrode sputtered on PTFE substrate and (b) those after the post electrochemical measurements. (c) Chronopotentiometry HER activity and corresponding H_2 signals measured on the Ag/PTFE electrode from -0.2 to -40 mA in Ar-saturated 0.05 M M_2CO_3 (M = Na, K, Cs) electrolytes. (d) DEMS calibration curve for H_2 as derived from the HER staircase. The error bars represent three independent measurements.

The collection efficiency of H_2 species from HER was first evaluated on the sputtered Ag electrode within Ar-saturated 0.05 M M_2CO_3 (M = Na, K, Cs) solutions. The signal of $m/z = 32$ was monitored to ensure the complete deaeration and thus exclude the potential faradaic current contribution from the oxygen reduction side reaction (Fig. S3, ESI†). As shown in Fig. 2c, a chronopotentiometry staircase was measured at a step length of 3 min and an HER current range from -0.2 to -40 mA, with the $m/z = 2$ mass-ion current recorded spontaneously as a representative of H_2 signal. Notably, given a constant DEMS operation pressure of 1×10^{-6} mbar and the same applied current, a similar H_2 signal was detected even upon different electrolyte switching, leading to a linear response between faradaic and mass-ion currents (Fig. 2d). Moreover, since H_2 and CO are the two predominant products generated from Ag catalyzed CO_2RR, this H_2 partial current calibration curve could be deployed for CO faradaic efficiency calculations on Ag by subtracting j_{H_2} from j_{total}, fulfilling the real-time quantitative analysis.

Comparison of GC and DEMS results of the cation effect study

Local electric field enhancement arising from the accumulation of specific hydrated cations at the outer Helmholtz plane (OHP) has been reported as an effective way to promote the CO_2RR activity for desired products, from both experimental approaches[45,46] and theoretical simulations.[47] Ringe *et al.* reported the effective interfacial cation size (radii) in the order of Cs^+ (3.5 Å) $<$ K^+ (4.1 Å) $<$ Na^+ (5.2 Å), the weakly hydrated cations such as Cs^+ are more concentrated at the OHP to induce a steeper potential gradient from the electrode surface to the OHP, which is also known as the electric field effect.[20] Herein, an online DEMS study on the cation identity effect on Ag catalyzed CO_2RR was performed at a temporal resolution of $\sim$200 ms to better interpret the dynamic reaction process.

Fig. 3a–c shows the chronoamperometric electrolysis results on the sputtered Ag electrode over carbon fiber paper substrate (Ag/CFP, Fig. S4, ESI†) in 0.1 M CO_2-saturated $MHCO_3$ (M = Na, K, Cs), the step duration at each potential was about 1 h for

752 | *Energy Environ. Sci.*, 2022, **15**, 749–759

This journal is © The Royal Society of Chemistry 2022

Fig. 3 The cation effect on CO_2RR as probed by online GC and DEMS. (a–c) Total current density and faradaic efficiencies for H_2 and CO products as derived from online GC measurements on Ag/CFP as averaged from 1 h continuous electrolysis within different electrolytes. (d–i) Real-time DEMS results of CO_2RR over the same Ag/PTFE electrode as recorded during linear sweep voltammetry from −0.6 V to −1.4 V *versus* RHE at a scan rate of 1 mV s^{-1}. The electrolyte can be simply switched from 0.1 M CO_2-saturated $NaHCO_3$ (blue line) to $KHCO_3$ (yellow line) and $CsHCO_3$ (red line) reservoir after each potential sweep, all the catholyte flow rates were kept at 128 mL min^{-1}.

3 continuous GC measurements, which were pre-calibrated using four standard gas mixtures (Fig. S5, ESI†). A significant H_2 suppression was observed at the potential below −0.6 V with the electrolyte switching from $NaHCO_3$ to $KHCO_3$ $CsHCO_3$, together with the maximum CO FE increasing from 37.2% to 86.1% and the j_{CO} increasing from −6.0 to −15.0 mA at around −1.26 V (Fig. S6, ESI†). This phenomenon is associated with the size of hydrated alkali cations and is in good agreement with earlier results.[45,46,48,49]

A set of DEMS measurements within different electrolytes were carried out on the same Ag/PTFE electrode with a linear potential sweep from −0.2 V to −1.4 V at a scan rate of 1 mV s^{-1}. The overall current density increases with increasing alkali cation size (Fig. 3d),[48] and the mass-ion currents of m/z = 2, 28 and 44 were recorded spontaneously as the representative of H_2, CO and CO_2, respectively (Fig. S7, ESI†). Notably, since the CO_2 reactant itself contains the fragment of 28 (Fig. S8, ESI†), a deconvolution of CO mass-ion signal was thus needed before the quantification of the CO_2RR products. A satisfied signal-to-noise ratio could be achieved at potentials around −0.6 V with a faradaic current of ∼−0.6 mA. Similar to the GC results, the H_2 FE gradually decreased from 96.9% to 22.7% with a negative potential sweep in $NaHCO_3$, and a more pronounced CO evolution activity was seen in the kinetic

regime from −0.7 to −0.9 V by switching to $KHCO_3$ and $CsHCO_3$ electrolytes (Fig. 3e and f). Some discrepancies on the determined CO FE and H_2 FE between these two methodologies were observed at a large overpotential regime below −1.1 V, which is probably attributable to the different mass transport limitations (Fig. S9, ESI†) within the H-cell and flow cell electrolyzer, respectively. Moreover, by plotting the mass-ion signal of 44 as a representative of CO_2 species, we could directly measure its utilization ratio during the negative potential sweep (Fig. 3g). Collecting the data in the $CsHCO_3$ electrolyte, for example, *ca.* 35% CO_2 was consumed at −1.4 V, which is 2-times higher than that in $NaHCO_3$. As a result, the partial current of j_{CO} recorded within $CsHCO_3$ at the given potential was twice that in $NaHCO_3$ electrolyte, while j_{H_2} is halved in the former (Fig. 3h and i). Chronoamperometric DEMS measurements were performed on the same sputtered Ag electrode within 0.1 M CO_2-saturated $MHCO_3$ at a flow rate of 128 mL min^{-1} and potential of −1.1 V for 1 h (Fig. S10, ESI†). A similar j_{H_2} was noted within the three electrolytes, while the j_{CO} increased from ∼−4 mA in $NaHCO_3$ to ∼−8 mA in $CsHCO_3$ together with a doubled depletion rate of aqueous CO_2 species, thus CO_2RR rather than HER contributes mainly to the overall enhanced faradaic current density in the Cs^+ electrolyte.

Another factor that can potentially contribute to enhancing the ratio of CO_2RR/HER is the increased local pH near the

cathode as arising from a higher OH^- generation rate (Fig. 3d of current density plot). To better differentiate the cation effect from the local pH effect on CO selectivity, we then focus on the kinetic regime wherein a minor current density variation is noted upon electrolyte switching from $NaHCO_3$ to $KHCO_3$ and $CsHCO_3$ over the same Ag/PTFE electrode. As shown in Table S1 (ESI†), the overall current density slightly increased from -2.34 mA in 0.1 M CO_2-saturated $NaHCO_3$ to -2.55 mA in $CsHCO_3$ electrolyte at -0.8 V, leading to a minor surface pH increment from 7.80 to 7.83. Nevertheless, the CO selectivity increased from 11.6% to 47.4% with the switching of the electrolyte from $NaHCO_3$ to $CsHCO_3$. In the earlier findings of Berlinguette et al.,[50] a 1.3-fold enhancement of CO faradaic efficiency was reported upon increasing ∼0.6 units of the surface pH. Herein, this 4-fold enhancement in CO selectivity is, therefore, mainly attributable to the local electric field effect from the cation identity rather than the neglectable surface pH increase by 0.03 units at the given potential within the kinetic regime.

To better illustrate the cation effect, we further compared the partial current densities for both H_2 and CO products recorded in different electrolytes with 3 different applied potentials in Fig. S11 (ESI†), a profound partial current enhancement to CO was noted upon the decrease in the effective interfacial cation size from Na^+ to Cs^+, while the formation rates of H_2 is less affected by the cation size. In an explicit model of the electrochemical interface, Nørskov et al. suggested that the interfacial electric field created by the hydrated alkali cations in the OHP aids in the stabilization of surface intermediates such as $^*CO_2$ and $^*COOH$ with significant dipole moments rather than $^*H$.[51] Our determined j_{CO} rather than j_{H_2} in DEMS measurements actually increases in the same order of the interfacial electric field strength as $Na^+ < K^+ < Cs^+$,

thus experimentally verifying this cation effect as their electrostatic interactions with the electric dipole of specific adsorbates.[49]

Electrochemical performance of plasma-treated Ag

The electrochemical reduction of the metal oxide precursor to generate surface defects and grain boundary-enriched metal catalysts has been proved as another effective strategy to regulate the desired CO_2 reduction over the proton reduction side reaction.[18,52] Herein, we pretreated the Ag/PTFE electrode with low-pressure O_2 plasma bombardment and comparatively carried out a DEMS investigation of the surface topology effect on CO_2RR performance. Fig. 4a and b depict the morphology change of the sputtered Ag/PTFE electrode, roughened Ag nanostructures can be clearly seen from SEM images after plasma bombardment (SEM images of Ag/CFP are shown in Fig. S12, ESI†), together with the color change from silver into golden brown. As shown in Fig. S13 (ESI†), the electrochemical double-layer capacitance of O_2 plasma-treated Ag electrodes is ca. 2.1 times that of pristine Ag, in line with SEM characterization and the enhanced roughness reports.[53,54] Along with earlier reports, a higher fraction of undercoordinated Ag sites is expected on the roughened surface that binds $^*COOH$ and $^*CO$ preferentially (vide infra).[55,56] In addition to the topology evolution, the surface composition change is also noticed after O_2 plasma bombardment. Fig. S14 (ESI†) shows the core-level XPS spectra of the Ag 3d region, the predominant Ag $3d_{5/2}$ peak shifts from 368.64 eV in the pristine Ag to 368.44 eV in the plasma-treated Ag, suggestive of the oxidation etching of metallic Ag^0 into Ag_2O.[18,57]

Prior to CO_2RR measurements, this plasma-treated Ag/PTFE electrode was electrochemically reduced and stabilized at -0.54 V vs. RHE for 1800 s (Fig. S15, ESI†). Then,
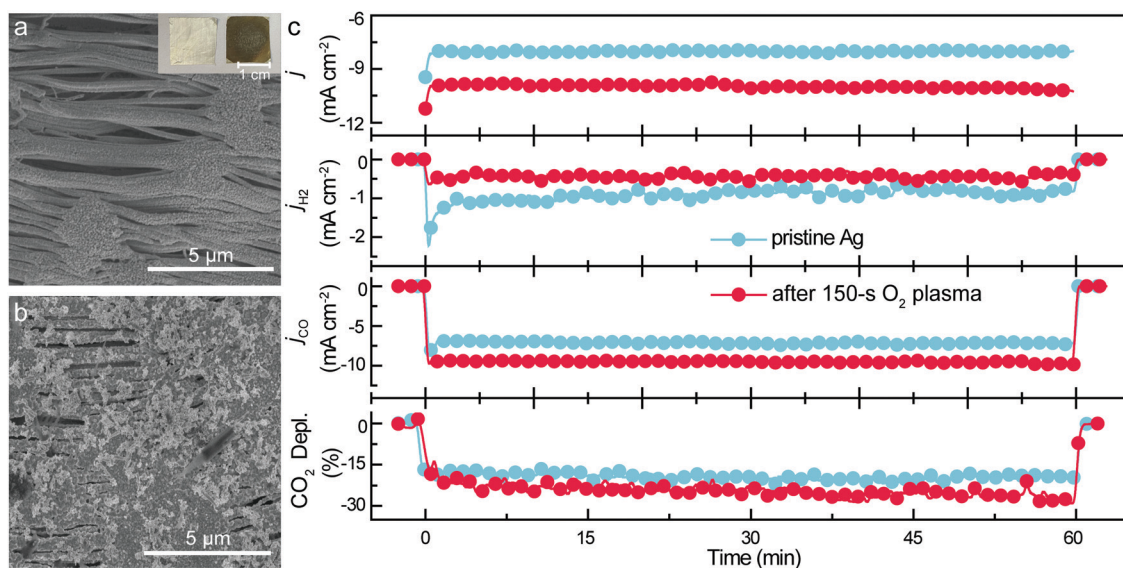

Fig. 4 Effect of O_2 plasma pre-treatment on Ag catalyzed CO_2RR. (a) SEM images for pristine and (b) 150 s O_2 plasma-treated Ag/PTFE electrodes. (c) Time-course of faradaic current densities, H_2 and CO partial currents as derived from DEMS signals recorded at -1.1 V versus RHE.

electrochemical CO_2 reduction during the negative potential sweep from -0.4 V to -1.4 V at a scan rate of 1 mV s^{-1} was investigated using DEMS as shown in Fig. S16 (ESI†), together with 1 h chronoamperometric measurement at -1.1 V within the 0.1 M CO_2-saturated $CsHCO_3$ (Fig. 4c). The current density increases from -8.0 mA on the pristine Ag/PTFE to -9.9 mA on the plasma-treated electrode at -1.1 V, moreover, a 23.5% increase in CO_2 conversion efficiency, a 33.8% higher j_{CO} and a suppressed j_{H_2} of 52.2% were noted on the latter as averaged from the 1 h electrolysis from DEMS approach. A similar trend was also observed for the O_2 plasma-treated Ag/CFP electrode (Fig. S17, ESI†).

In our recent work on plasma-bombarded Cu foil electrodes,[56] it was demonstrated that the plasma pre-treatments not only roughened the electrode surface but also gave rise to a modified surface topology, generating more coordination-unsaturated surface sites for regulating the reaction pathway. Herein, the determined Tafel slope within kinetic-controlled regime from DEMS measurements decreased from 116 mV dec^{-1} on the pristine Ag to 68 mV dec^{-1} on the

roughened Ag (Fig. S18, ESI†), experimentally verifying the role of under-coordinated Ag sites in lowering the *COOH activation barrier and thus improving CO evolution kinetics, which is in good agreement with previous reports on oxide-derived Au[52] and nanoporous Ag[15] catalyst, reinforcing the surface topology effect on enhancing CO_2RR performance.

Optimized CO_2RR device performance

In brief, the aforementioned local reaction environment study reveals three promotion effects of (1) CO_2 mass transport, (2) cation identity and (3) surface topology on improving CO_2RR performance in aqueous electrolytes. Thereafter, we further adopt a gas-fed CO_2 electrolyzer with anion exchange membrane electrode assembly (MEA) configuration to overcome the CO_2 mass transport limitation and the competitive HER side reaction at large overpotentials (Effect 1).[4,58–60] As illustrated in Fig. 5a and Fig. S19 (ESI†), a humidified CO_2 flow is supplied on the cathodic side of 1.5×1.5 cm^2 the O_2-plasma bombarded Ag/gas diffusion electrode (Ag/GDE, Effect 3) using an upstream rotameter and the effluent was delivered into the
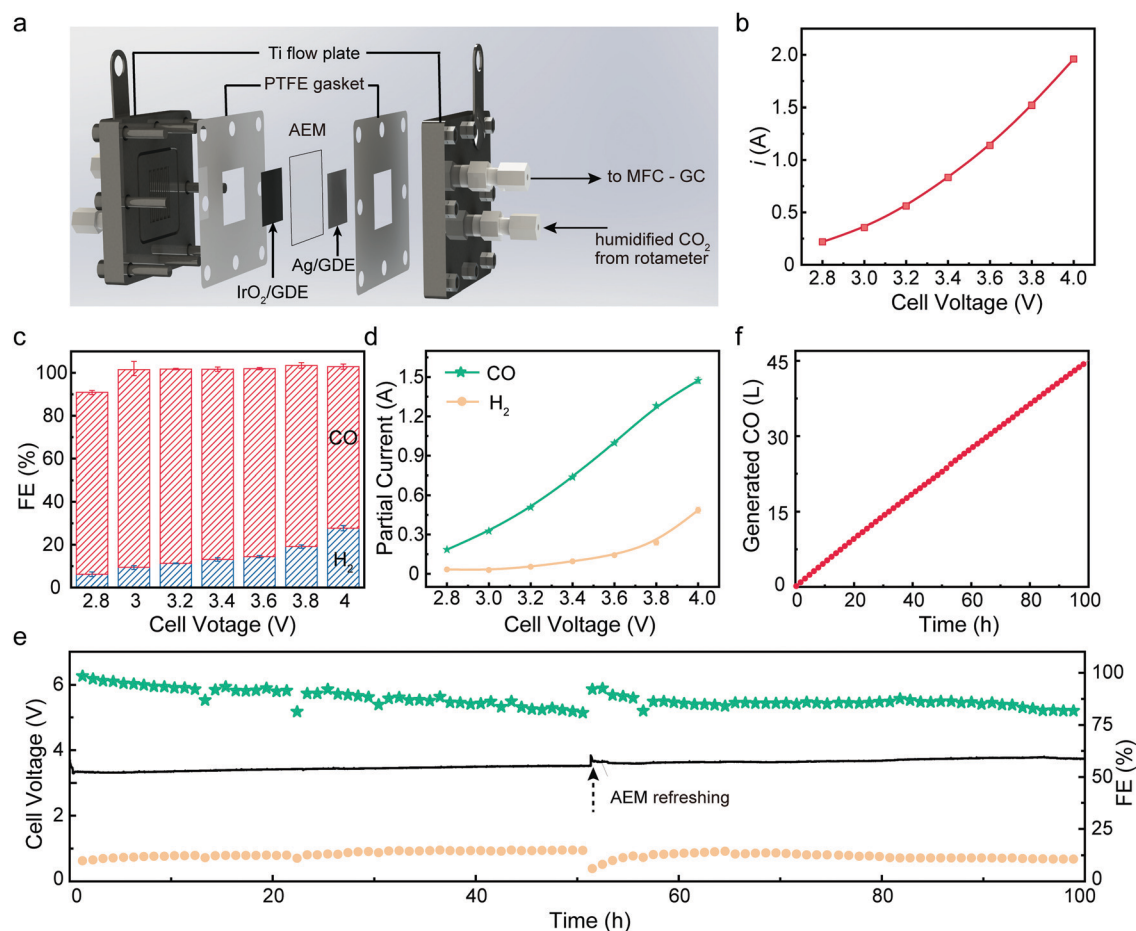
Fig. 5 CO_2RR performance upgrading with optimized local reaction environment. (a) Schematic of the anion exchange MEA electrolyzer. (b) Steady-state currents, (c) the corresponding faradaic efficiencies and (d) partial currents of CO and H_2 products recorded on O_2 plasma pre-treated Ag/GDE cathode at each applied voltage without iR-correction. (e) Long-term electrolysis at a constant current density of 500 mA cm^{-2}, (f) the accumulated CO volume during 100 h continuous electrolysis.

This journal is © The Royal Society of Chemistry 2022

Energy Environ. Sci., 2022, **15**, 749–759 | **755**

GC for quantitative analysis at a rate of 100 sccm as monitored by the mass flow controller, refraining from the FE overestimation due to CO_2 consumption.[61,62] The electrolyte circulation takes place only on the anode side of IrO_2/GDE to keep the membrane wetting as well as to carrying out O_2 bubbles from water oxidation (see Materials).

Fig. 5b shows the steady-state current recorded at each applied voltage with 10 mM CsOH anolyte, for which the overall current increased from 0.18 A at 2.8 V to 1.95 A at 4.0 V without iR-compensation. Moreover, a wide potential window over 1.0 V was noted for maintaining the high CO FE of above 80%, with a maximum selectivity of up to 92% at 3.0 V and a j_{CO} partial current exceeding 0.65 A cm^{-2} at 4.0 V (Fig. 5c and d), which is among the best reported MEA performance so far (Table S2 and Fig. S20, ESI†). A more detailed performance screening using either Milli-Q water or Cs_2CO_3, CsOH or KOH at the same molar concentration was comparatively carried out and the results are plotted in Fig. S21 and S22 (ESI†). The same cation effect of Cs^+, as compared to K^+, on promoting CO evolution activity was noted even in this anion exchange membrane setup (Effect 2), mainly due to the inevitable cation cross-over through the membrane as reported by Janáky *et al.* in their most recent work.[63] Taken together, this superb CO_2-to-CO conversion performance could be ascribed to the synergy of the optimized mass transport of high c_{CO_2} but low $c_{H_2O,vapor}$, the increased surface roughness from oxide-derived Ag, and local electric field from the optimized cation identity. Last but not the least, we evaluated the long-term stability of this anion MEA electrolyzer for continuous CO generation with a constant current density of 500 mA cm^{-2} (or an overall current of 1.125 A). The chronopotentiometric curve is shown in Fig. 5e, for which, the cell voltage gradually increased from 3.32 V to 3.52 V at 50 h and further to 3.71 V at 100 h, while CO selectivity stayed above 90% in the first 13 hours and was maintained above 80% within the 100 h continuous electrolysis at the industrial-scale current density. Compared to the earlier report on the $KHCO_3$ anolyte,[64] no salt precipitation was observed neither within the internal architecture of Ag/GDE nor within the flow panel after the long-term operation (Fig. S23, ESI†), likely due to the lower cation concentration together with the 3-fold enhanced solubility of $CsHCO_3$ compared to $KHCO_3$. As a result, a total CO volume above 45 L was generated (Fig. 5f) in this 1.5×1.5 cm^2 prototype reactor.

Conclusion

In conclusion, we have presented an *operando* differential electrochemical mass spectroscopic approach to investigate the effect of the local reaction environment on the performance of CO_2 reduction using the Ag electrode as a stereotype. Through a combined numerical simulation and experimental design, our DEMS results suggest facile CO_2 mass transport, the larger interfacial electric field from the optimized cation identity, in coupling with the surface topology regulating from O_2 plasma bombardment and following electro-reduction, could largely boost the CO_2-to-CO conversion performance, which is in agreement with previous experimental and theoretical literature. As a proof of concept, these fundamental understandings have been validated in a modular anion exchange membrane electrolyzer, leading to an operational voltage window wider than 1.0 volts and a stable CO generation for 100 hours at 500 mA cm^{-2} for CO selectivity above 80%. The present methodology bridging interfacial spectroelectrochemistry with upgraded pilot performance could open an avenue for future renewable energy infrastructure, aiding in closing the anthropogenic carbon cycle.

Materials and methods

Electrode preparation

The working electrodes of *ca.* 400 nm Ag film sputtered on either PTFE membrane (20 μm pore size, Cobetter) or CFP (HCP010N, Hesen) substrates were prepared using a Technol JCP350 system, at a deposition rate of 2 Å s^{-1} to an effective thickness of 400 nm under 0.5 Pa Ar atmosphere (99.999%, Air Liquide). The Ag loading was determined as ∼0.27 mg cm^{-2}. Prior to the magnetron sputtering, the hydrophobic PTFE membrane was pre-treated with acetone, methanol and Milli-Q water (18.2 MΩ cm) in succession and dried in a stream of flowing N_2 (99.999%, Keju Chemistry). For O_2 plasma pre-treatment, the Ag/PTFE or Ag/CFP electrodes were placed in an HM-Plasma2L (Hongming Instrument), evacuated with a mechanical pump to ∼10 torr, and then got exposed to a 150 W plasma for 150 s under 80 sccm O_2 flow (99.999%, Air Liquide).

Material characterizations

The surface morphology images were filmed using an FEI Sirion 200 field-emission scanning electron microscopy (SEM), using an electron beam energy of 5 kV and a spot size of 3.0 nm with magnification ranging from 5 to 80k. The near-surface composition of Ag electrodes was probed using X-ray photoelectron spectroscopy (XPS) with a Kratos AXIS Ultra DLD spectrometer, using a monochromatic Al Kα radiation (1486.6 eV) and a low energy flood gun as a neutralizer. Casa XPS program was employed for surface componental content analysis where the binding energies were calibrated by referencing the C 1s peak at 284.8 eV. The morphology characterization using MicroCT was performed on a Zeiss Xradia 520 Versa X-ray microscope. The distances of the sample to the X-ray source (13.5 mm) or the X-ray detector (77 mm) resulted in a voxel (volume pixel) size of 1 μm. The field of view was approximately 1020.2 μm × 1020.2 μm, and the reconstruction of MicroCT data was conducted using the TXM Reconstructor software (Xradia).

Electrochemical measurements

Electrochemical CO_2RR measurements on Ag/CFP were performed in a customized gastight H-type glass cell separated by Nafion 117 membrane (Fuel Cell Store). A high-purity graphite rod (99.995%, Aldrich) and a saturated calomel electrode

756 | *Energy Environ. Sci.*, 2022, **15**, 749–759

This journal is © The Royal Society of Chemistry 2022

(SCE, CH Instruments) were employed as the counter and reference electrodes, respectively. Certain amounts of M_2CO_3 (M = Na, K or Cs, 99.99%, Damas-Beta) were dissolved in Milli-Q water toward the same concentration of 0.05 M, which was further purified by electrolysis between two graphite rods at 0.1 mA for 24 h to remove trace amounts of metal ion impurities. Prior to bulk electrolysis, 50 sccm CO_2 (99.995%, Air Liquide) was bubbled for at least 30 min to obtain the 0.1 M CO_2-saturated $MHCO_3$ electrolyte. Electrochemical responses were recorded on a Biologic VSP-300 potentiostat. The solution resistance (R_u) was determined using potentiostatic electrochemical impedance spectroscopy (PEIS) at frequencies ranging from 0.1 Hz to 200 kHz, and manually compensated as E (iR-corrected $vs.$ RHE) = E ($vs.$ RHE) − $R_u \times i$ (amps of averaged current). All potentials (if not specifically mentioned) in this work were converted to the RHE scale as E ($vs.$ RHE) = E ($vs.$ SCE) + 0.244 V + 0.0591 $\times$ pH$_{bulk}$ and E ($vs.$ RHE) = E ($vs.$ Ag/AgCl) + 0.197 V + 0.0591 $\times$ pH$_{bulk}$.

CO_2RR product quantification

The effluent from the electrochemical cell was analyzed using a Shimadzu 2014 gas chromatography (GC) equipped with a thermal conductivity detector (TCD) for H_2 concentration quantification and a flame ionization detector (FID) coupled with a methanizer for quantifying CO concentration. UHP Ar was used as the carrier gas and constituents of the gaseous sample were separated using two Porapak N80/100 columns packed with molecular sieve-13X. The signal responses of TCD and FID were calibrated by analyzing a series of standard gas mixtures (Wetry, H_2 concentrations of 50.6, 505, 7557, 101 000 ppm and CO concentrations of 20.3, 203, 7510, 50 100 ppm). Faradaic efficiency (FE) of certain reduction products was calculated as:

$$FE_i = \frac{x_i v n F}{V \times j} \times 100\%$$

where x_i is the volume fraction of specie i as determined by on-line GC, v is the flow rate, generally set at 20 or 50 sccm depending on the total current density and being monitored by an Alicat mass flow controller, n is the electron transfer number, F is the faradaic constant, V is the molar volume of an ideal gas under CO_2RR operation condition, j is the total current density.

DEMS measurements

On-line DEMS measurements were run on a Hiden HPR-40 quadrupole mass spectrometer equipped with a secondary electron multiplier detector. A cage voltage of 3 V, electron energy of 70 eV and an emission current of 500 μA were set at the ionization source, together with a detector voltage of 900 V for recording real-time mass spectra. Prior to data acquisition, DEMS background signals were pre-stabilized for 1 h and were subtracted from m/z signals for quantitative analysis. The working pressure was set at $\sim$1.0 $\times$ 10^{-6} mbar for all DEMS measurements. The setup of the DEMS system is illustrated in Fig. 1 and the flow-cell was machined with polyether-ether-ketone (PEEK) material, consisting of a 1.13 cm^{-2} Ag/PTFE working electrode, Pt gauze (99.9%, Sigma) counter electrode, and leak-free Ag/AgCl (Innovative Instruments Inc.) as the reference electrode. Prior to each experiment, the PEEK cells were sonicated with 20 wt% nitric acid and boiled in Milli-Q water for cleaning.

MEA measurements

For the practical membrane electrode assembly electrolyzer tests, a 1.5 $\times$ 1.5 cm^2 Ag/GDE (Toray TGP-H-060 with microporous layer) pre-treated with 150 s O_2 plasma was used as the CO_2RR cathode and IrO_2 (P40V020, Premetek Co.) air-brushed onto Toray TGP-H-060 GDE was used as the anode at a $\sim$2.0 mg cm^{-2} loading. A quaternary ammonia poly(N-methyl-piperidine-co-p-terphenyl) (QAPPT, EVE Energy) anion exchange membrane was sandwiched by two gas diffusion electrodes to separate the chambers. The QAPPT membrane was pre-activated in 1 M KOH at 60 °C for 24 h prior to usage. Two PTFE gaskets were placed in between cathodic and anodic flow plates to avoid short-circuiting. A 100 sccm humidified CO_2 was delivered through the cathodic Ti flow field in the absence of the catholyte, while the anolyte, either Milli-Q water or 10 mM $KOH/CsOH/Cs_2CO_3$, was circulated at a flow rate of 1.8 mL min^{-1}.

Conflicts of interest

The authors declare no conflict of interest.

Acknowledgements

References

1 N. S. Lewis and D. G. Nocera, *Proc. Natl. Acad. Sci. U. S. A.*, 2006, **103**, 15729–15735.

2 Z. W. Seh, J. Kibsgaard, C. F. Dickens, I. Chorkendorff, J. K. Norskov and T. F. Jaramillo, *Science*, 2017, **355**, 6321.

3 C. Hepburn, E. Adlen, J. Beddington, E. A. Carter, S. Fuss, N. Mac Dowell, J. C. Minx, P. Smith and C. K. Williams, *Nature*, 2019, **575**, 87–97.

4 R. G. Grim, Z. Huang, M. T. Guarnieri, J. R. Ferrell, L. Tao and J. A. Schaidle, *Energy Environ. Sci.*, 2020, **13**, 472–494.

5 S. Verma, B. Kim, H. R. Jhong, S. Ma and P. J. Kenis, *ChemSusChem*, 2016, **9**, 1972–1979.

6 M. Jouny, W. Luc and F. Jiao, *Ind. Eng. Chem. Res.*, 2018, **57**, 2165–2177.

This journal is © The Royal Society of Chemistry 2022

Energy Environ. Sci., 2022, **15**, 749–759 | **757**

7   O. S. Bushuyev, P. De Luna, C. T. Dinh, L. Tao, G. Saur, J. van de Lagemaat, S. O. Kelley and E. H. Sargent, *Joule*, 2018, **2**, 825–832.

8   S. Nitopi, E. Bertheussen, S. B. Scott, X. Liu, A. K. Engstfeld, S. Horch, B. Seger, I. E. L. Stephens, K. Chan, C. Hahn, J. K. Norskov, T. F. Jaramillo and I. Chorkendorff, *Chem. Rev.*, 2019, **119**, 7610–7672.

9   Y. Y. Birdja, E. Pérez-Gallent, M. C. Figueiredo, A. J. Göttle, F. Calle-Vallejo and M. T. M. Koper, *Nat. Energy*, 2019, **4**, 732–745.

10 S. Jin, Z. Hao, K. Zhang, Z. Yan and J. Chen, *Angew. Chem., Int. Ed.*, 2021, **60**, 2–24.

11 E. L. Clark and A. T. Bell, *J. Am. Chem. Soc.*, 2018, **140**, 7012–7020.

12 F. Zhang and A. C. Co, *Angew. Chem., Int. Ed.*, 2020, **59**, 1674–1681.

13 N. Hoshi, M. Kato and Y. Hori, *J. Electroanal. Chem.*, 1997, **440**, 283–286.

14 E. L. Clark, S. Ringe, M. Tang, A. Walton, C. Hahn, T. F. Jaramillo, K. Chan and A. T. Bell, *ACS Catal.*, 2019, **9**, 4006–4014.

15 Q. Lu, J. Rosen, Y. Zhou, G. S. Hutchings, Y. C. Kimmel, J. G. Chen and F. Jiao, *Nat. Commun.*, 2014, **5**, 3242.

16 Y. Yoon, A. S. Hall and Y. Surendranath, *Angew. Chem., Int. Ed.*, 2016, **55**, 15282–15286.

17 J. Rosen, G. S. Hutchings, Q. Lu, S. Rivera, Y. Zhou, D. G. Vlachos and F. Jiao, *ACS Catal.*, 2015, **5**, 4293–4299.

18 M. Ma, B. J. Trzesniewski, J. Xie and W. A. Smith, *Angew. Chem., Int. Ed.*, 2016, **55**, 9748–9752.

19 A. Dutta, C. E. Morstein, M. Rahaman, A. Cedeño López and P. Broekmann, *ACS Catal.*, 2018, **8**, 8357–8368.

20 S. Ringe, E. L. Clark, J. Resasco, A. Walton, B. Seger, A. T. Bell and K. Chan, *Energy Environ. Sci.*, 2019, **12**, 3001–3014.

21 S. S. Bhargava, F. Proietto, D. Azmoodeh, E. R. Cofell, D. A. Henckel, S. Verma, C. J. Brooks, A. A. Gewirth and P. J. A. Kenis, *ChemElectroChem*, 2020, **7**, 2001–2011.

22 C. M. Gunathunge, V. J. Ovalle and M. M. Waegele, *Phys. Chem. Chem. Phys.*, 2017, **19**, 30166–30172.

23 A. Thevenon, A. Rosas-Hernández, A. M. Fontani Herreros, T. Agapie and J. C. Peters, *ACS Catal.*, 2021, **11**, 4530–4537.

24 A. D. Handoko, F. Wei Jenndy, B. S. Yeo and Z. W. Seh, *Nat. Catal.*, 2018, **1**, 922–934.

25 X. Li, S. Wang, L. Li, Y. Sun and Y. Xie, *J. Am. Chem. Soc.*, 2020, **142**, 9567–9581.

26 C. W. Li and M. W. Kanan, *J. Am. Chem. Soc.*, 2012, **134**, 7231–7234.

27 K. P. Kuhl, E. R. Cave, D. N. Abram and T. F. Jaramillo, *Energy Environ. Sci.*, 2012, **5**, 7050–7059.

28 N. Heidary, K. H. Ly and N. Kornienko, *Nano Lett.*, 2019, **19**, 4817–4826.

29 N. J. Firet and W. A. Smith, *ACS Catal.*, 2016, **7**, 606–612.

30 J. Li, X. Chang, H. Zhang, A. S. Malkani, M. J. Cheng, B. Xu and Q. Lu, *Nat. Commun.*, 2021, **12**, 3264.

31 F. S. Roberts, K. P. Kuhl and A. Nilsson, *Angew. Chem., Int. Ed.*, 2015, **54**, 5179–5182.

32 J. Li, X. Li, C. M. Gunathunge and M. M. Waegele, *Proc. Natl. Acad. Sci. U. S. A.*, 2019, **116**, 9220–9229.

33 A. Javier, B. Chmielowiec, J. Sanabria-Chinchilla, Y.-G. Kim, J. H. Baricuatro and M. P. Soriaga, *Electrocatalysis*, 2015, **6**, 127–131.

34 B. Hasa, M. Jouny, B. H. Ko, B. Xu and F. Jiao, *Angew. Chem., Int. Ed.*, 2021, **60**, 3277–3282.

35 K. J. P. Schouten, Y. Kwon, C. J. M. van der Ham, Z. Qin and M. T. M. Koper, *Chem. Sci.*, 2011, **2**, 1902–1909.

36 K. J. Schouten, Z. Qin, E. Perez Gallent and M. T. Koper, *J. Am. Chem. Soc.*, 2012, **134**, 9864–9867.

37 E. L. Clark, M. R. Singh, Y. Kwon and A. T. Bell, *Anal. Chem.*, 2015, **87**, 8013–8020.

38 P. Khanipour, M. Loffler, A. M. Reichert, F. T. Haase, K. J. J. Mayrhofer and I. Katsounaros, *Angew. Chem., Int. Ed.*, 2019, **58**, 7273–7277.

39 M. Löffler, P. Khanipour, N. Kulyk, K. J. J. Mayrhofer and I. Katsounaros, *ACS Catal.*, 2020, **10**, 6735–6740.

40 C. J. Bondue, M. Graf, A. Goyal and M. T. M. Koper, *J. Am. Chem. Soc.*, 2021, **143**, 279–285.

41 H. Baltruschat, *J. Am. Soc. Mass Spectrom.*, 2004, **15**, 1693–1706.

42 S. M. Aftab, A. S. Mohd Rafie, N. A. Razak and K. A. Ahmad, *PLoS One*, 2016, **11**, e0153755.

43 J. Bredberg, S.-H. Peng and L. Davidson, *Int. J. Heat Fluid Flow*, 2002, **23**, 731–743.

44 L. R. De Souza Jr and L. Lorenz, Proc. COMSOL Conf., 2014.

45 J. Resasco, L. D. Chen, E. Clark, C. Tsai, C. Hahn, T. F. Jaramillo, K. Chan and A. T. Bell, *J. Am. Chem. Soc.*, 2017, **139**, 11277–11287.

46 A. Malkani, J. Li, N. Oliveira, M. He, X. Chang, B. Xu and Q. Lu, *Sci. Adv.*, 2020, **6**, eabd2569.

47 D. Bohra, J. H. Chaudhry, T. Burdyny, E. A. Pidko and W. A. Smith, *Energy Environ. Sci.*, 2019, **12**, 3380–3389.

48 M. R. Singh, Y. Kwon, Y. Lum, J. W. Ager, 3rd and A. T. Bell, *J. Am. Chem. Soc.*, 2016, **138**, 13006–13012.

49 M. C. O. Monteiro, F. Dattila, B. Hagedoorn, R. García-Muelas, N. López and M. T. M. Koper, *Nat. Catal.*, 2021, **4**, 654–662.

50 Z. Zhang, L. Melo, R. P. Jansonius, F. Habibzadeh, E. R. Grant and C. P. Berlinguette, *ACS Energy Lett.*, 2020, **5**, 3101–3107.

51 L. D. Chen, M. Urushihara, K. Chan and J. K. Nørskov, *ACS Catal.*, 2016, **6**, 7133–7139.

52 Y. Chen, C. W. Li and M. W. Kanan, *J. Am. Chem. Soc.*, 2012, **134**, 19969–19972.

53 Y. W. Choi, F. Scholten, I. Sinev and B. Roldan Cuenya, *J. Am. Chem. Soc.*, 2019, **141**, 5261–5266.

54 W. Tang, A. A. Peterson, A. S. Varela, Z. P. Jovanov, L. Bech, W. J. Durand, S. Dahl, J. K. Norskov and I. Chorkendorff, *Phys. Chem. Chem. Phys.*, 2012, **14**, 76–81.

55 Y. Chen, Y. Huang, T. Cheng and W. A. Goddard, 3rd, *J. Am. Chem. Soc.*, 2019, **141**, 11651–11657.

56 K. Jiang, Y. Huang, G. Zeng, F. M. Toma, W. A. Goddard and A. T. Bell, *ACS Energy Lett.*, 2020, **5**, 1206–1214.

57 X.-Y. Gao, S.-Y. Wang, J. Li, Y.-X. Zheng, R.-J. Zhang, P. Zhou, Y.-M. Yang and L.-Y. Chen, *Thin Solid Films*, 2004, **455–456**, 438–442.

758 | *Energy Environ. Sci.*, 2022, **15**, 749–759

This journal is © The Royal Society of Chemistry 2022

58 M. G. Kibria, J. P. Edwards, C. M. Gabardo, C. T. Dinh, A. Seifitokaldani, D. Sinton and E. H. Sargent, *Adv. Mater.*, 2019, **31**, e1807166.

59 D. Gao, P. Wei, H. Li, L. Lin, G. Wang and X. Bao, *Acta Phys.- Chim. Sin.*, 2020, 2009021.

60 D. A. Salvatore, C. M. Gabardo, A. Reyes, C. P. O'Brien, S. Holdcroft, P. Pintauro, B. Bahar, M. Hickner, C. Bae, D. Sinton, E. H. Sargent and C. P. Berlinguette, *Nat. Energy*, 2021, **6**, 339–348.

61 M. Ma, E. L. Clark, K. T. Therkildsen, S. Dalsgaard, I. Chorkendorff and B. Seger, *Energy Environ. Sci.*, 2020, **13**, 977–985.

62 Z.-Z. Niu, L.-P. Chi, R. Liu, Z. Chen and M.-R. Gao, *Energy Environ. Sci.*, 2021, **14**, 4169–4176.

63 B. Endrodi, A. Samu, E. Kecsenovity, T. Halmagyi, D. Sebok and C. Janaky, *Nat. Energy*, 2021, **6**, 439–448.

64 Y. Xu, J. P. Edwards, S. Liu, R. K. Miao, J. E. Huang, C. M. Gabardo, C. P. O'Brien, J. Li, E. H. Sargent and D. Sinton, *ACS Energy Lett.*, 2021, **6**, 809–815.

This journal is © The Royal Society of Chemistry 2022

Energy Environ. Sci., 2022, **15**, 749–759 | **759**